PHYSICAL REVIEW B, VOLUME 65, 184301

Raman spectroscopy of $CaMnO_3$: Mode assignment and relationship between Raman line intensities and structural distortions

M. V. Abrashev,[1,2] J. Bäckström,[2,*] L. Börjesson,[2] V. N. Popov,[1] R. A. Chakalov,[3] N. Kolev,[4] R.-L. Meng,[4] and M. N. Iliev[4]

[1]*Faculty of Physics, University of Sofia, BG-1164 Sofia, Bulgaria*

[2]*Department of Applied Physics, Chalmers University of Technology and Göteborg University, 41296 Göteborg, Sweden*

[3]*School of Physics and Astronomy, The University of Birmingham, Edgbaston, Birmingham B15 2TT, United Kingdom*

[4]*Texas Center for Superconductivity, University of Houston, Houston, Texas 77204-5932*

(Received 9 November 2001; revised manuscript received 31 January 2002; published 15 April 2002)

Polarized Raman spectra of oriented finely twinned $CaMnO_3$ thin films and nonpolarized Raman spectra of $CaMnO_3$ ceramics were studied at room temperature using several excitation laser wavelengths. The selection rules for the polarized Raman spectra, obtained from samples consisting of finely twinned orthorhombic domains, were calculated and the symmetry of all observed Raman lines was determined. The relationship between the intensity of the Raman lines and the distortions in the ABO_3 perovskites with $GdFeO_3$-type structure is discussed. These distortions can be described as superposition of four simple basic distortions: two MnO_6 octahedral tilts, Jahn-Teller deformation of Mn^{3+} O_6 octahedra, and shift of the A ions from their sites in the ideal perovskite. Twenty of the 24 Raman-allowed modes in the real $GdFeO_3$-type structure have counterparts in *only one* of the four simpler structures, obtained by a single basic distortion. The assignment of the Raman lines of $CaMnO_3$ to definite atomic vibrations, most of them activated by a single basic distortion, was made in close comparison with the results of lattice dynamical calculations and the Raman spectra of isostructural $LaMnO_3$ and $CaGeO_3$.

DOI: 10.1103/PhysRevB.65.184301 PACS number(s): 78.30.Hv, 63.20.Dj, 68.55.Jk

I. INTRODUCTION

The phenomenon *colossal magnetoresistance* (CMR), characterized by strong interplay of structural, magnetic, and transport properties, is most clearly pronounced in mixed-valence perovskite manganites $R_{1-x}A_xMnO_3$ ($R=$rare earth element, $A=$Ca, Sr, Ba, Pb, . . .), and $La_{1-x}Ca_xMnO_3$ is one of the most studied CMR systems.[1] In the past few years there have been several reports on the structure of these materials, in particular on their structural transformation upon doping and temperature variation near the temperatures of the magnetic phase transitions.[1,2] Ca^{2+} has an ionic radius of 1.34 Å, i.e., very close to that of La^{3+} of 1.36 Å. Unlike other perovskite manganites, the averaged structure of $La_{1-x}Ca_xMnO_3$ remains orthorhombic in the entire substitutional range at temperatures below ~700 K. However, the radii of $Mn^{3+}(t_{2g}^3e_g^1)$ and $Mn^{4+}(t_{2g}^3)$, which coexist at intermediate values of x, differ significantly. Mn^{3+} (0.58 Å), which is a Jahn-Teller (JT) ion, is larger than the non-Jahn-Teller Mn^{4+} (0.53 Å). Furthermore, the e_g electron of Mn^{3+} has an orbital degree of freedom. While the superexchange coupling between Mn^{4+} is antiferromagnetic, the superexchange interaction between Mn^{3+} ions depends on the relative orbital ordering and can be antiferromagnetic or ferromagnetic. In addition, there is a ferromagnetic coupling between Mn^{3+} and Mn^{4+} through the double-exchange mechanism. All this results in a complicated phase diagram, reflecting the sensitive interrelations of charge carrier concentration, magnetic couplings, and structural distortions.

The experimental data accumulated so far provide strong evidence that at a microscopic level the structure of $La_{1-x}Ca_xMnO_3$ can be described within a single-crystallographic phase only for the limiting cases $x=0$ and $x=1$. To some extent this could be true also for compounds corresponding to $x=N/8$ ($N=1,3,4,5$), where commensurate charge and orbital ordering at low temperatures have been experimentally confirmed.[3] In the general case, in particular at low temperatures, the structure of $La_{1-x}Ca_xMnO_3$ rather consists of coexisting domains of different phases with relative weight that varies with doping, temperature, and applied magnetic field. It is reasonable to assume that the structure of these phases is closely related to those of $LaMnO_3$, $La_{0.5}Ca_{0.5}MnO_3$, and $CaMnO_3$, although definite differences due to dynamical reduction of the Jahn-Teller distortion in the ferromagnetic conducting state or disorder of the type of Jahn-Teller-liquid or Jahn-Teller-glass in the insulating state may occur. In any case, the identification of these phases and the monitoring of their mutual transformations are essential for understanding the correlations between structural, magnetic, and transport properties of manganites.

Raman spectroscopy is among the few experimental techniques capable to detect coexisting domains of size, comparable to the lattice constant. The identification of microphases in $La_{1-x}Ca_xMnO_3$ requires a good knowledge of the spectra of $LaMnO_3$, $La_{0.5}Ca_{0.5}MnO_3$, and $CaMnO_3$ and of the effects of particular lattice distortions on the Raman spectra. The spectra of orthorhombic $LaMnO_3$ are well known.[4] Recently, the spectra of $La_{0.5}Ca_{0.5}MnO_3$ have also been analyzed.[5] In this work we present and analyze the polarized Raman spectra of $CaMnO_3$ using a more general approach. This approach is based on the fact that the lattice distortions in the ABO_3 perovskites of $GdFeO_3$-type structure can be described as a superposition of four simple basic distortions: two MnO_6 octahedral tilts, Jahn-Teller deformaion of $Mn^{3+}O_6$ octahedra, and a shift of the *A* ions from their sites in the ideal perovskite. Twenty of the 24 Raman-allowed modes in the real $GdFeO_3$-type structure have counterparts in only one of the four simpler structures obtained by a single basic distortion. Therefore, neglecting resonance effects, the intensity of most of the Raman lines is determined mainly by the magnitude of *only one* basic distortion. On the basis of such considerations, the results of lattice dynamical calculations and by comparison with the spectra of isostructural $LaMnO_3$ and $CaGeO_3$, the Raman lines of $CaMnO_3$ were assigned to definite phonon modes.

II. EXPERIMENT

A. Samples

Thin films of $CaMnO_3$ were deposited on single-crystal substrates of $SrTiO_3$ and $LaAlO_3$ with quasicubic (100) surface orientation by laser ablation of single ceramic target with stoichiometric composition. A Lambda-Physik LPX210 krypton-fluorine excimer laser (wavelength 248 nm, pulse length 30 ns, repetition rate 5 Hz) was used to deliver a flow of 1.5 J/cm^2 per pulse within a 2×4 mm^2 spot on the target surface. The substrate was positioned on a heated holder against the ablated material plasma plume at a distance of 75 mm. To ensure highly oriented growth, the substrate was kept at 780 °C during the deposition. The ablation was carried out in oxygen at a pressure of 40 Pa, which was found to be optimal for the plasma plume formation. After the deposition, the chamber was filled with oxygen up to 0.9 atm and the samples were slowly cooled down with a rate of 10 °C/min. The last step was taken to prevent oxygen loss from the film. Under these conditions, the deposition rate was 0.05 nm/pulse and the film thickness was ≈ 150 nm.

The film crystal lattice quality was investigated by x-ray diffraction (XRD) with a Bruker D5000 four-circle diffractometer. In both cases $CaMnO_3/LaAlO_3$ and $CaMnO_3/SrTiO_3$, only (00l) reflections from the films were observed in the Θ-2Θ diffraction patterns, which evidences highly ordered crystal lattice in the direction perpendicular to the substrate surface plane (100). In-plane epitaxial growth was confirmed by φ-scan XRD. The peaks resulting from the film lattice fourfold symmetry matched the corresponding peaks from the substrates and no other peaks were registered. Omega-scan XRD (rocking curves) was used to compare the crystal lattice perfection of the two films. The full width at half maximum (FWHM) of $CaMnO_3$ (002) reflections revealed that the film grown on $LaAlO_3$ substrate is slightly better ordered (FWHM = 0.36°) than the film grown on $SrTiO_3$ (FWHM = 0.40°).

The ceramic samples of $CaMnO_3$ were prepared by solid-state reaction of CaO and MnO_2. A 1:1 stoichiometric powder mixture of the oxides was calcinated in air at 900 °C for 16 h. The material was reground twice, pressed, and sintered in air at 1100 °C for 16 h. The lattice parameters, as determined by x-ray powder diffraction, were in agreement with Ref. 6.

TABLE I. Shell model parameters.

Ion	Z ($\lvert e\rvert$)	Y ($\lvert e\rvert$)	α (Å^3)	Ionic pair	a (eV)	b (Å^{-1})	c (eV Å^6)
Ca	1.90	3.5	1.5	Ca-O	840	2.72	0
Mn	3.80	2.3	0.01	Mn-O	900	2.67	0
O	−1.90	−3.0	2.0	O-O	22764	6.710	20.37

B. Raman spectroscopy and lattice dynamical calculations

The Raman spectra were measured using a Dilor XY800 triple-grating spectrometer equipped with a microscope and liquid-nitrogen-cooled charge-coupled device detector. Six lines in the range of photon energies from 1.83 eV (676 nm) to 2.71 eV (458 nm) from an Ar^+-Kr^+ laser were used for excitation. A 100× objective was used to both focus the incident laser beam onto a spot of about 2 μm in diameter and to collect the scattered light in a backscattering geometry. The laser power on the spot was kept at 1 mW for all wavelengths. The polarization of the incident laser light was selected with the use of an achromatic half-wavelength plate and a polarizer filter. The scattered light was analyzed using a second polarizer filter. At all experimental conditions additional reference spectra from a metallic mirror (for removal of the plasma lines), from a single crystal of silicon (for correction of the different sensitivity of the spectrometer in different scattering configurations), and from a single crystal of BaF_2 (for correction of the sensitivity of the spectrometer for different laser excitation wavelengths) were collected.

The lattice-dynamical calculations (LDC's) of $CaMnO_3$ are accomplished within a shell model.[7] This predominantly ionic compound is described in this model as a three-dimensional system of point charges Z which interact with each other through Coulomb interactions. The repulsion of the electron subsystems of the neighboring ions is described by introducing short-range forces of the Born-Mayer-Buckingham form

$$V = a\exp(-br) - \frac{c}{r^6}, \tag{2.1}$$

where a, b, and c are parameters, and r is the interionic separation. Finally, a simple model of the deformability of the electron shells of the ions is used in which an ion is represented as a point charged core with charge $Z-Y$ coupled with a force constant k to a charged massless shell with charge Y around it. The free ion polarizability α is then given by

$$\alpha = \frac{Y^2}{k}. \tag{2.2}$$

The values of model parameters (listed in Table I) for Ca and O were taken from Ref. 7 and for Mn were derived by use of the equilibrium conditions.

III. RESULTS AND DISCUSSION

A. Determination of the symmetry of the Raman lines

Polarized Raman spectra of $CaMnO_3$ thin film deposited on $LaAlO_3$ substrate are shown in Figs. 1(a)–1(d) in four different scattering configurations (xx, $y'x'$, $x'x'$ and yx) for four (488, 515, 568, and 647 nm) laser excitation wavelengths. The first and second symbols in the Porto's notations, indicating the scattering configuration, are the direction of the polarization of the incident and scattered light, respectively, where x, y, x', and y' are parallel to the quasicubic [100], [010], [110], and $[\bar{1}10]$ crystal directions. The xx-$x'x'$ and yx-$y'x'$ pairs of spectra are essentially different: evidence that the investigated thin film is oriented. On the other hand, attempts to find different types spectra for xx and yy (or $x'x'$ and $y'y'$) polarizations failed, indicating that the thin film is finely twinned on the scale of the laser spot size.

The symmetry of a Raman line can be determined by its presence, absence, or change in the relative intensity in spectra measured in some exact scattering configurations (with polarizations of the incident and scattered light along some simple crystallographic directions). We calculated the intensities of all types of Raman-active modes in the polarization configurations used, accounting for the six possible orientations of the $Pnma$ orthorhombic twins in the laboratory system, connected with the quasicubic axes.[8] It was assumed that the scattering volumes for the twins of each orientation are equal (i.e., no texturing) and that the medium is optically quasi-isotropic (weak dependence of the refractive index on the crystal direction). The results are shown in Table II.[9] As it follows from Table II, depending on the variations of the intensities in the four experimental scattering configurations, the Raman lines can be divided into three groups. The lines corresponding to modes of B_{1g} and B_{3g} symmetry are undistinguishable and they both should be observed with equal intensities only in $x'x'$ and yx configurations. For B_{2g} modes the ratio of the intensities in the xx, $y'x'$, and $x'x'$ spectra should be 4:3:1 and they are not allowed in the yx spectra. As the Raman tensor for the A_g modes contains three independent parameters, the A_g lines may have different intensity ratio in the four types of spectra and only the simplest cases are given in Table II.[10,11] Using Table II we can assign the lines at 564, 320, and 179 cm^{-1} to modes of B_{1g} or B_{3g} symmetry, the lines at 465 and 258 cm^{-1} to B_{2g} modes, and the remaining lines at 615, 487, 438, 382, 322, 278, 243, 184, 160, and 150 cm^{-1} to A_g symmetry.

The Raman spectra obtained from the other $CaMnO_3$ thin film deposited on $SrTiO_3$ substrate contained lines located at the same wave numbers; i.e., none of the observed lines is substrate related.[12] For the latter film, however, there was a tendency for equalization of the spectra in parallel (xx and $x'x'$) and crossed (yx and $y'x'$) polarizations and for a deviation from the selection rules of Table II. This indicates a break of domain orientation, which is not unexpected as the mismatch between the quasicubic lattice constants of $CaMnO_3$ and $SrTiO_3$ is larger (4.8%, $a_{CMO}=3.73$ Å, $a_{STO}=3.91$ Å) compared to that between $CaMnO_3$ and $LaAlO_3$ (1.6%, $a_{LAO}=3.79$ Å).

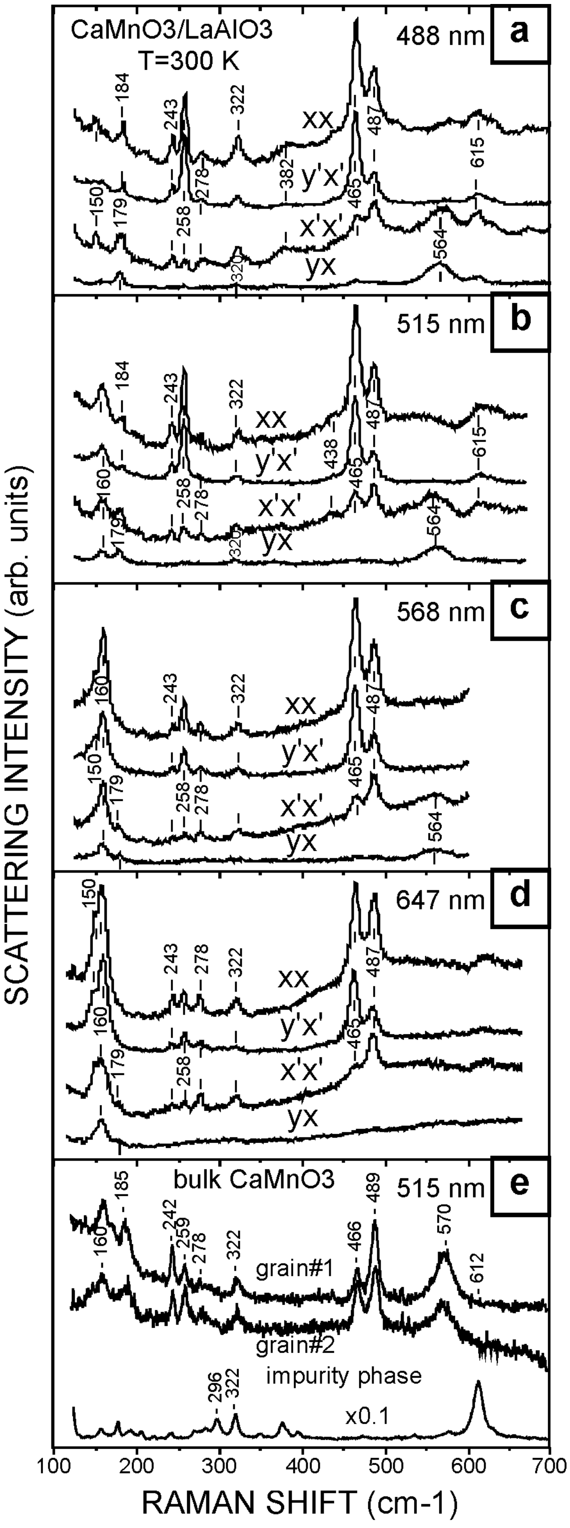

FIG. 1. Polarized Raman spectra at room temperature obtained from the surface of $CaMnO_3$ thin film on $LaAlO_3$ substrate with different laser wavelength (a) 488 nm, (b) 515 nm, (c) 568 nm, and (d) 647 nm. The scattering configuration for each spectrum is indicated. x, y, x', and y' are parallel to the quasicubic [100], [010], [110], and $[\bar{1}10]$ directions, respectively. The bottom panel (e) shows the nonpolarized spectra of bulk $CaMnO_3$ and of an impurity phase.

TABLE II. Calculated intensities (in arbitrary units) of the Raman lines in different polarization geometries. a,b, and c are the nonzero components of the Raman tensor of A_g modes.

Symmetry of the modes	Polarization $xx \equiv yy$	$y'x'$	$x'x' \equiv y'y'$	yx
B_{1g} or B_{3g}	0	0	1	1
B_{2g}	4	3	1	0
A_g $(a=b=c)$	1	0	1	0
A_g $(a=c \ll b)$	2	1	1	0
A_g $(a=c \gg b)$	4	1	3	0

Some of the Raman lines exhibit strong resonant behavior. The intensity of the 487, 278, and 160 cm^{-1} lines increases with the increasing excitation wavelength. The lines at 564, 322, 258, 243, 184, and 179 cm^{-1} show opposite behavior. It appears that an appropriate laser line for simultaneous observation of all Raman lines of $\mathrm{CaMnO_3}$ is 515 nm. By chance this laser line is most often used and our 515 nm Raman spectra and those obtained with 515 nm line from $\mathrm{CaMnO_3}$ ceramic samples by Liarokapis *et al.*[13] and Granado *et al.*[14,15] are very similar. The only difference is the additional line at 615 cm^{-1} in our thin-film spectra. The 615 cm^{-1} line, however, was absent in spectra measured from grains of unknown orientation in $\mathrm{CaMnO_3}$ ceramics [see Fig. 1(e)]. Instead, the ceramics contains an unidentified yellow-reddish impurity phase. The Raman spectrum of this phase contains a very intense line at 612 cm^{-1}, indicating that the presence of the 615 cm^{-1} in the thin-film spectra is due to a secondary phase.

B. Model of the basic structural distortions

In this section, the effect of the structural distortions on the intensity of the Raman lines will be discussed. The stoichiometric $\mathrm{CaMnO_3}$ and $\mathrm{LaMnO_3}$ crystallize in the $\mathrm{GdFeO_3}$-type structure,[16] described by the $Pnma$ space group (D_{2h}^{16}, No. 62). This structure can be considered as orthorhombically distorted superstructure of the ideal cubic $AB\mathrm{O}_3$ perovskite and its unit cell ($\sqrt{2}a_p \times 2a_p \times \sqrt{2}a_p$) contains four formula units (ideal perovskite unit cells) (see Fig. 2). La(Ca), Mn, O(1), and O(2) occupy sites with C_s^{xz}, C_i, C_s^{xz}, and C_1 site symmetry, respectively (see Table III). The Mn atoms do not participate in the 24 $(7A_g+5B_{1g}+7B_{2g}+5B_{3g})$ Raman-allowed phonon modes. Due to the atomic site symmetries, 5 out the 12 atomic coordinates are fixed. The $Pnma$ structure can thus be considered as having seven structural degrees of freedom [La(Ca) (2), Mn (0), O(1) (2), O(2) (3)].[17] The atomic coordinates can be rewritten in a form where the variables are the difference between the real coordinate and the coordinate in the ideal cubic perovskite structure, so that these variables can be regarded as perturbations. The change of each of these seven variables, however, leads to distorted structures without simple physical meaning. However, they can be grouped into four groups in such a manner that the variation of the new "variables" (further called "basic distortions") will result in superstructures with well-defined lattice distortions.

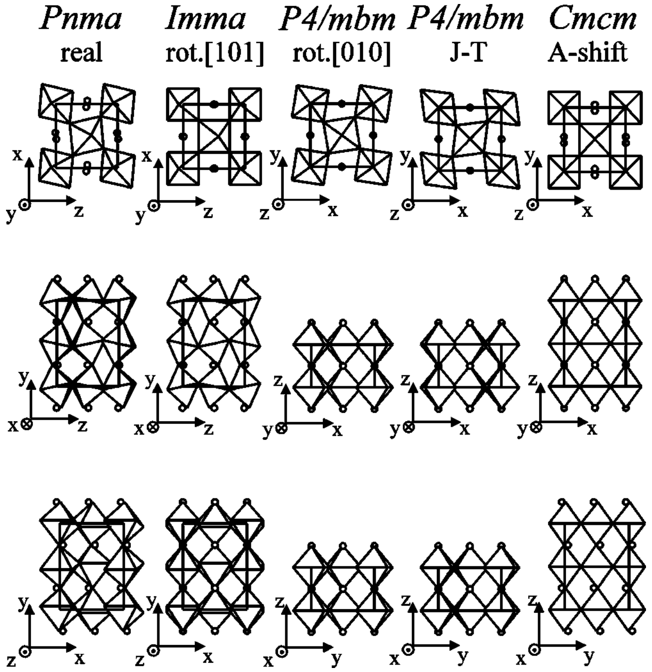

FIG. 2. The $\mathrm{GdFeO_3}$-type crystal structure and the four simpler structures obtained from only one of the proposed basic distortions.

The *first* basic distortion $D_{[101]}$, which includes three of the variables, is a rotation (tilt) of the $\mathrm{MnO_6}$ octahedra considered as rigid polyhedra around the [101] cubic axis. The resulting structure is orthorhombic (space group $Imma$) with body-centered unit cell $\sqrt{2}a_p \times 2a_p \times \sqrt{2}a_p$ (see Table III and Fig. 2). The quantitative measure of $D_{[101]}$ is the angle of the rotation. If the distortion is small, the angle of rotation is equal to $2\sqrt{2}|z_{O(1)}|$ (or $4\sqrt{2}|y_{O(2)}|$ as if the octahedra are rigid, $|z_{O(1)}|=2|y_{O(2)}|$).

The *second* basic distortion $D_{[010]}$ is a rotation of the $\mathrm{MnO_6}$ octahedra, considered again as rigid polyhedra, around the [010] cubic axis. The resulting structure is tetragonal (space group $P4/mbm$) with unit cell $\sqrt{2}a_p \times \sqrt{2}a_p \times a_p$ (in the tetragonal basis). The measure of $D_{[010]}$ is again the angle of rotation, which, if the distortion is small, is equal to $2|x_{O(2)}-z_{O(2)}|$ (in the $Pnma$ basis). The crystallographic reason for these rotational-like distortions is the mismatch between the ionic radius r_a of the A-site atoms (La or Ca) and the ionic radius r_{Mn} of Mn measured by the tolerance factor $t=(r_a+r_O)/\sqrt{2}(r_{Mn}+r_O)$ of the perovskitelike structure.

The classification of the perovskite distortions in terms of tilts of rigid octahedra has been made by Glazer[18] and the simple structures, obtained by only the first or only the second basic distortion, have Glazer notations (a^-0a^-) and $(0b^+0)$, respectively. Note, however, that the symmetry of the $Imma$ space group requires only the octahedra to have four equal Mn-O(2) distances. The Mn-O(2) and Mn-O(1) bonds can be different and the O(2)-Mn-O(2) and O(1)-Mn-O(2) angles can differ from 90°. The symmetry of the second space group $P4/mbm$, requires four equal Mn-O(2) bonds and right O(2)-Mn-O(2) and O(1)-Mn-O(2) angles, but allows for the Mn-O(1) and Mn-O(2) distances to be different.

TABLE III. Wyckoff notation, site symmetry, and atomic position of the atoms in the real crystal structure with space group *Pnma* and in the four simpler crystal structures, containing only one of the four basic distortions (given in brackets). The orientation of the crystal axes is standard for each space group. For better comparison of the unit cells in all cases Mn is in the origin of the coordinate system. The atomic positions are rewritten in a form, where *x*, *y*, and *z* are small parameters.

Space group, basic distortion and unit cell	A = La, Ca	B = Mn	O(1) (apex)	O(2) (plane)
Pnma (real) $\sqrt{2}a_p \times 2a_p \times \sqrt{2}a_p$	4c C_s^{xz} $x_A, \frac{1}{4}, \frac{1}{2}+z_A$	4a C_i 0, 0, 0	4c C_s^{xz} $x_{O(1)}, \frac{1}{4}, z_{O(1)}$	8d C_1 $\frac{1}{4}+x_{O(2)}, y_{O(2)}, \frac{1}{4}+z_{O(2)}$
Imma (rot. [101]) $\sqrt{2}a_p \times 2a_p \times \sqrt{2}a_p$	4e C_{2v}^{z} $0, \frac{1}{4}, \frac{1}{2}+z_A$	4a C_{2h}^{x} 0, 0, 0	4e C_{2v}^{z} $0, \frac{1}{4}, z_{O(1)}$	8g C_2^{y} $\frac{1}{4}, y_{O(2)}, \frac{1}{4}$
*P*4/*mbm* (rot. [010]) $\sqrt{2}a_p \times \sqrt{2}a_p \times a_p$ [a]	2c D_{2h}' $\frac{1}{2}, 0, \frac{1}{2}$	2a C_{4h} 0, 0, 0	2b C_{4h} $0, 0, \frac{1}{2}$	4g C_{2v}' $\frac{1}{4}+x_{O(2)}, \frac{1}{4}-x_{O(2)}, 0$
*P*4/*mbm* (JT) $\sqrt{2}a_p \times \sqrt{2}a_p \times a_p$ [a, b]	2b C_{4h} $\frac{1}{2}, 0, \frac{1}{2}$	2d D_{2h}' 0, 0, 0	2c D_{2h}' $0, 0, \frac{1}{2}$	4g C_{2v}' $\frac{1}{4}+x_{O(2)}, \frac{1}{4}+x_{O(2)}, 0$
Cmcm (*A* shift) $\sqrt{2}a_p \times \sqrt{2}a_p \times 2a_p$ [a]	4c C_{2v}^{y} $\frac{1}{2}, y_A, \frac{1}{4}$	4a C_{2h}^{x} 0, 0, 0	4c C_{2v}^{y} $0, y_{O(1)}, \frac{1}{4}$	8d C_i $\frac{1}{4}, \frac{1}{4}, 0$

[a] The *x*, *y*, and *z* axes of this cell correspond to the *z*, *x*, and *y* axes in the *Pnma* cell, respectively.

[b] Nonstandard origin.

It means that, in fact, our model does not need the oversimplification of regarding the MnO_6 octahedra as rigid.

The *third* basic distortion D_{JT} is a deformation of the MnO_6 octahedra so that the $Mn(O(2))_4$ square transforms to a rhomb. The resulting structure is tetragonal (space group $P4/mbm$) with unit cell $\sqrt{2}a_p \times \sqrt{2}a_p \times a_p$ (in the tetragonal basis; see Fig. 2). The measure of D_{JT} is the relative difference of the two pairs of Mn-O(2) distances $\Delta d_{Mn\text{-}O(2)}/\langle d_{Mn\text{-}O(2)} \rangle$. If the distortion is small, it is equal to $2|x_{O(2)}+z_{O(2)}|$ (in the *Pnma* basis). In the case of Mn^{3+} ions ($LaMnO_3$) this distortion originates from the Jahn-Teller effect, caused by the presence of one electron in the degenerate e_g orbital of the Mn^{3+} ion.

The *fourth* basic distortion $D_{A-shift}$ is a shift of the *A*-type atoms from their sites in the ideal perovskite in *x* direction (in the *Pnma* basis). The resulting structure is also orthorhombic, but with base-centered unit cell $\sqrt{2}a_p \times \sqrt{2}a_p \times 2a_p$ described by the *Cmcm* space group (in different orthorhombic basis compared with the one of the real *Pnma* structure; see Fig. 2 and Table III). The origin for such a shift can be understood if the oxygen environment of the *A*-type atoms is considered. In the ideal cubic perovskite the *A* atom is bonded to 12 oxygens with equal bonds (12-fold environment). The first three of the above described basic distortions change the environment of the *A* atoms, but in all cases it remains an even number (the *A*-O bonds are distributed in pairs[19]). The $D_{A\text{-}shift}$ transforms the oxygen environment of the *A* atom into odd-fold one, making two *A*-O(1) bonds in the *x* direction (in *Pnma* basis) the shortest and longest ones, respectively. The reason for such a change can be stereochemical (some peculiarity of the electronic configuration of the valence shell of the *A* atom) or crystallographic (large mismatch between the ionic radius of the *A* atoms and the radius of the cavity between the 12 oxygens, with a center in the place of the *A* atom in the ideal cubic perovskite).

TABLE IV. Comparison of the values of the basic distortions in several perovskites.

Compound	$D_{[101]}$		$D_{[010]}$	D_{JT}	$D_{A\text{-}shift}$	Ref.
	$2\sqrt{2}\lvert z_{O(1)}\rvert$	$4\sqrt{2}\lvert y_{O(2)}\rvert$	$2\lvert x_{O(2)}-z_{O(2)}\rvert$	$2\lvert x_{O(2)}+z_{O(2)}\rvert$	$2x_A$	
$YMnO_3$ (300 K)	0.4302	0.3366	0.1984	0.0268	0.1610	4
$LaMnO_3$ (300 K)	0.2107	0.2172	0.1620	0.0644	0.0980	20
$LaMnO_3$ (798 K)	0.1943	0.2184	0.1204	0.0120	0.0434	20
$La_{0.75}Ca_{0.25}MnO_3$ (240 K)	0.1839	0.1908	0.1058	0.0030	0.0428	21
$La_{0.75}Ca_{0.25}MnO_3$ (20 K)	0.1810	0.1880	0.1056	0.0028	0.0426	21
$CaMnO_3$ (300 K)	0.1865	0.1900	0.1503	0.0012	0.0666	6
$CaGeO_3$ (300 K)	0.1714	0.1810	0.1346	0.0026	0.0566	22

TABLE V. Correlation table between cubic zone-boundary modes (in the ideal $Pm\overline{3}m$ structure), corresponding to Raman-active modes in the real orthorhombic $Pnma$ structure, and the corresponding Raman-active modes in the simpler structures, containing only one basic distortion. The last column contains calculated frequencies for the Raman-active modes in $CaMnO_3$.

Symmetry in $Pm\overline{3}m$	Symmetry in $Pnma$	Corresponding modes in simpler structures				Calc. freq. in $CaMnO_3$ (cm^{-1})
		$Imma$ rot. [101]	$P4/mbm$ rot. [010]	$P4/mbm$ Jahn-Teller	$Cmcm$ A shift	
R_1	$\rightarrow B_{3g}(1)$	B_{3g}	–	–	–	754
M_1	$\rightarrow B_{2g}(1)$	–	–	B_{2g}	–	749
X_1	$\rightarrow B_{1g}(1)$	–	–	–	B_{3g}	743
M_3	$\rightarrow A_g(1)$	–	B_{1g}	A_{1g}	–	555
R_{12}	$\rightarrow B_{3g}(2)$	B_{3g}	–	–	–	541
	$\searrow B_{1g}(2)$	B_{1g}	–	–	–	536
M_4	$\rightarrow B_{2g}(2)$	–	B_{2g}	–	–	485
	$\nearrow A_g(3)$	A_g	–	–	–	467
R'_{25}	$\rightarrow B_{3g}(3)$	B_{3g}	–	–	–	459
	$\searrow B_{2g}(3)$	B_{2g}	–	–	–	453
X_5	$\rightarrow B_{2g}(6)$	–	–	–	B_{1g}	366
	$\searrow A_g(6)$	–	–	–	A_g	345
X_1	$\rightarrow B_{1g}(5)$	–	–	–	B_{3g}	354
M_5	$\rightarrow B_{3g}(4)$	–	$\rightarrow E_g$	$\rightarrow E_g$	–	304
	$\searrow B_{1g}(4)$	–	$\nearrow$	$\nearrow$	–	281
	$\nearrow A_g(5)$	A_g	–	–	–	299
R'_{25}	$\rightarrow B_{2g}(5)$	B_{2g}	–	–	–	292
	$\searrow B_{3g}(5)$	B_{3g}	–	–	–	290
X_5	$\rightarrow A_g(7)$	–	–	–	A_g	242
	$\searrow B_{2g}(7)$	–	–	–	B_{1g}	232
	$\nearrow A_g(4)$	A_g	–	–	–	200
R'_{15}	$\rightarrow B_{1g}(3)$	B_{1g}	–	–	–	178
	$\searrow B_{2g}(4)$	B_{2g}	–	–	–	148
M_2	$\rightarrow A_g(2)$	–	A_{1g}	B_{1g}	–	154

In Table IV the calculated basic distortions (using structural data from the literature) for some perovskites related to $CaMnO_3$ are listed. While $D_{[101]}$, $D_{[010]}$, and $D_{A\text{-}shift}$ in these compounds are comparable (excluding the orthorhombic $YMnO_3$), D_{JT} varies significantly.

C. Group-theoretical analysis and lattice-dynamical calculations results

Following Daniel *et al.*[23] and using the relations between the lattice vectors of the orthorhombic $GdFeO_3$-type structure with space group $Pnma$ (regarded as weakly distorted) and the lattice vectors of the cubic perovskite, it can be shown that the vibrational modes located at the $\Gamma_o(0,0,0)$ point of the othorhombic Brillouin zone come from modes located at the $\Gamma_c(0,0,0)$, $R_c(\frac{1}{2},\frac{1}{2},\frac{1}{2})$, $M_c(\frac{1}{2},0,\frac{1}{2})$, and $X_c(0,\frac{1}{2},0)$ points of the cubic Brillouin zone, where R_c, M_c, and X_c are zone-boundary points. The Raman-active modes in the orthorhombic $Pnma$ structure [only part of all vibrational modes the $\Gamma_o(0,0,0)$ point] originate only from the cubic zone-boundary points R_c, M_c, and X_c and the correlation table is shown in Table V (for the labeling of the cubic vibrational modes, see Ref. 23).

The results of our lattice dynamical calculations for $CaMnO_3$ are shown in Table V and Fig. 3. Using them we determined exactly the correspondence between the Raman-active $Pnma$ modes and the cubic zone-boundary modes (for the numbering of the othorhombic modes, see Fig. 3). On the other hand, in the two simpler tetragonal $P4/mbm$ structures, the four Raman-active modes are of different symmetry and the vibrational pattern of the modes can be determined using only group-theoretical methods. For the two simpler orthorhombic $Imma$ and $Cmcm$ structures there is more than one Raman-active mode from each type of symmetry, but in this case the linear combination of the symmetry coordinates having the closest vibrational pattern to one of the modes from the orthorhombic $Pnma$ structure can be constructed. Having all these results, the one-to-one correspondence between the cubic zone-boundary modes, the Raman-active modes in the $Pnma$ structure of $CaMnO_3$, and the Raman-active modes in the four simpler structures, containing only one of the four basic distortions, can be made (see Table V). Using Table V we made some general conclusions. First, the frequencies of the $Pnma$ modes, originating from a split degenerated cubic zone-boundary mode, are close. This justifies the approach to the distortions in the

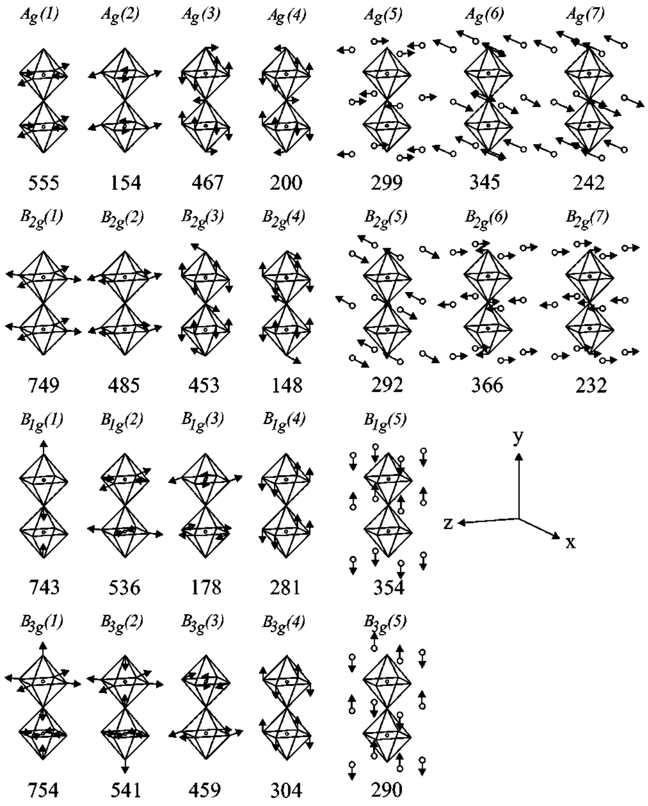

FIG. 3. Vibrational patterns of the Raman-active modes in the $GdFeO_3$-type structure (in the case of $CaMnO_3$). The labeling of the modes follows Ref. 4.

$GdFeO_3$-type structure as to small perturbations. The second finding is that 20 out of 24 Raman-active $Pnma$ modes have an Raman-active counterpart in *only one* of the simpler structures obtained from one basic distortion. Therefore, at out-of-resonance conditions, the intensity of each of these 20 modes can be used as a measure of the magnitude of the basic distortion activating the mode. Two of the remaining four modes, $A_g(1)$ and $A_g(2)$, have Raman-active counterparts in both tetragonal structures, but the corresponding modes have different symmetry in them (A_{1g} and B_{1g}, respectively). In this case the measured ratio of the nonzero parameters in the Raman tensor of the mode can be used to determine the dominating basic distortion.[24] The other two of the remaining four modes, $B_{1g}(4)$ and $B_{3g}(4)$, have double-degenerated E_g counterpart in both tetragonal structures.

D. Raman line assignment and comparison to related compounds

A tentative assignment of the observed Raman lines of $CaMnO_3$ using the results of lattice-dynamical calculations is given in Table VI. First, we point out that there are more experimentally observed lines of A_g symmetry (see Fig. 1) than predicted by group theory. Out of the A_g lines only that at 612 cm^{-1} can unambiguously be treated as a spurious line connected with traces of an impurity phase. The weak lines at 382 and 438 cm^{-1} also seem to be of different origin since their frequencies differ significantly from the calculated frequencies for the A_g modes. The assignment is somewhat ambiguous in the frequency range below 200 cm^{-1}. While only two A_g lines are expected from the LDC's, three lines were observed there. We tentatively assign the lines at 160 and 184 cm^{-1} to the two proper $A_g(2)$ and $A_g(4)$ low-frequency modes. The assignment of the lines of B_{1g} and B_{3g} symmetry is also rather ambiguous due to the impossibility to use scattering configurations where B_{1g} or B_{3g} are separately pronounced. Only the line at 179 cm^{-1} can easily be associated with the $B_{1g}(3)$ mode with calculated frequency 178 cm^{-1}. The assignment of 320 and 564 cm^{-1} lines to B_{3g} modes is rather arbitrary. These lines may as well represent B_{1g} modes.

As follows from Table VI, the strong lines in the Raman spectra of $CaMnO_3$ correspond to modes activated by the $D_{[101]}$ and $D_{A\text{-}shift}$ basic distortions. This is in striking contrast to the Raman spectra of $LaMnO_3$,[4] where the most intensive $B_{2g}(1)$ line at 611 cm^{-1} is activated by the D_{JT} basic distortion. A line corresponding to the $B_{2g}(1)$ mode is not even observed in the spectra of $CaMnO_3$. The explanation of this fact is simple accounting for the values of basic distortions (see Table IV): the D_{JT} basic distortion in $LaMnO_3$ is almost 60 times larger than in $CaMnO_3$. This justifies the earlier suggestion[12,28] that the intensity of the $\sim$611 cm^{-1} line in manganites is governed by the Jahn-Teller distortions.

The structures of $CaMnO_3$ and $CaGeO_3$ have close values of the basic distortions (see Table IV). For this reason, similar relative intensities in the corresponding Raman spectra could be expected. Indeed, such a similarity is seen if the polarized Raman spectra of $CaGeO_3$ (see Fig. 2a in Ref. 27) and $CaMnO_3$ (Fig. 1) are compared. On the other hand, most of the weak lines in one of the compounds have no counterpart in the other (see Table VI). This fact could be explained by the strong resonant behavior of some Raman modes, clearly seen in Fig. 1. It appears that the proposed dependence of the Raman line intensities on the above-defined basic perovskite distortions can only partially help to determine the origin of the Raman lines in the case of manganites. Better predictions of the model can be expected for transparent perovskites with $GdFeO_3$ structure, where resonant effects are negligible.

IV. CONCLUSIONS

The polarized Raman spectra of oriented $CaMnO_3$ thin films and nonpolarized Raman spectra of polycrystalline $CaMnO_3$ bulk samples were measured at room temperature using several laser lines. The symmetry of the Raman lines was determined making use of recalculated selection rules for the case of finely twinned $Pnma$ structure. The analysis of the spectra and the assignment of Raman lines to definite atomic vibrations was done on the basis of symmetry considerations, lattice-dynamical calculations, and by comparison with the Raman spectra of isostructural $LaMnO_3$ and $CaGeO_3$. We argue that the relative intensity of some Raman lines can be used as a measure for the basic distortions in perovskites with $GdFeO_3$-type structure.

TABLE VI. Comparison of the calculated and the experimental frequencies of the Raman-active modes in $CaGeO_3$, $CaMnO_3$, and $LaMnO_3$. The numbering of the modes follows Ref. 4 and Fig. 3. Bold font numbers indicate Raman lines with highest intensity. The basic distortion, activating the mode, is indicated in the last column.

Mode symmetry and number	$CaGeO_3$ Calc. Ref. 26	$CaGeO_3$ Expt. Ref. 27	$CaMnO_3$ Calc. This paper	$CaMnO_3$ Expt.	$LaMnO_3$ Calc. Ref. 4	$LaMnO_3$ Expt.	Activating distortion
$A_g(1)$	507	–	555	–	582	–	rot. [010], JT
$A_g(3)$	480	–	467	**487**	480	**493**	rot. [101]
$A_g(6)$	329	**328**	345	322	263	–	A-shift
$A_g(5)$	292	**284**	299	278	162	198	rot. [101]
$A_g(7)$	257	265	242	243	81	140	A-shift
$A_g(4)$	169	**171**	200	184	326	**284**	rot. [101]
$A_g(2)$	147	**151**	154	160	246	257	rot. [010], JT
$B_{2g}(1)$	524	–	749	–	669	**611**	JT
$B_{2g}(2)$	497	526	485	–	509	–	rot. [010]
$B_{2g}(3)$	372	–	453	**465**	464	481	rot. [101]
$B_{2g}(6)$	297	–	366	–	369	308	A-shift
$B_{2g}(5)$	250	–	292	–	150	170	rot. [101]
$B_{2g}(7)$	225	248	232	**258**	123	109	A-shift
$B_{2g}(4)$	161	162	148	–	218	–	rot. [101]
$B_{1g}(1)$	557	–	743	–	693	–	A-shift
$B_{1g}(2)$	413	–	536	–	575	–	rot. [101]
$B_{1g}(5)$	387	358	354	–	182	184	A-shift
$B_{1g}(4)$	351	237	281	–	347	–	rot. [010], JT
$B_{1g}(3)$	230	184	178	179	254	–	rot. [101]
$B_{3g}(1)$	568	–	754	–	692	–	rot. [101]
$B_{3g}(2)$	500	496	541	**564**	603	–	rot. [101]
$B_{3g}(3)$	429	380	459	–	462	–	rot. [101]
$B_{3g}(4)$	329	–	304	320	343	320	rot. [010], JT
$B_{3g}(5)$	179	–	290	–	158	–	rot. [101]

ACKNOWLEDGMENTS

Support for this work was provided by the Swedish Foundation for Strategic Research and by the University of Sofia through Project No. 3344. The work of R.-L.M, N.K., and M.N.I. was supported by the state of Texas through the Texas Center for Superconductivity and in part by the MRSEC Program of NSF under Grant No. DMR-9632667.

---

*Present address: Inst. für Angewandte Physik, Universität Hamburg, Jungiusstr. 11, 20355 Hamburg, Germany.

[1] See, e.g., D.I. Khomskii and G.A. Sawatzky, Solid State Commun. **102**, 87 (1997); J.M.D. Coey, M. Viret, and S. von Molnar, Adv. Phys. **48**, 167 (1999).

[2] *Colossal Magnetoresistive Oxides*, edited by Yoshinori Tokura, Advances in Condensed Matter Science, Vol. 2 (Gordon and Breach, Amsterdam, 2000).

[3] C.-W. Cheong and C.H. Chen, in *Colossal Magnetoresistance, Charge-ordering and Related Aspects of Manganese Oxides*, edited by C.N.R. Rao and B. Raveau (World Scientific, Singapore, 1998), p. 241.

[4] M.N. Iliev, M.V. Abrashev, H.-G. Lee, V.N. Popov, Y.Y. Sun, C. Thomsen, R.L. Meng, and C.W. Chu, Phys. Rev. B **57**, 2872 (1998).

[5] M.V. Abrashev, J. Bäckström, L. Börjesson, M. Pissas, N. Kolev, and M.N. Iliev, Phys. Rev. B **64**, 144429 (2001).

[6] K.R. Poeppelmeier, M.E. Leonowicz, J.C. Scanlon, J.M. Longo, and W.B. Yelon, Solid State Chem. **45**, 71 (1982).

[7] V. Popov, J. Phys.: Condens. Matter **7**, 1625 (1995), and references therein.

[8] R. Wang, J. Gui, Y. Zhu, and A.R. Moodenbaugh, Phys. Rev. B **63**, 144106 (2001).

[9] Note that the ratio of the calculated intensities is the same as for the lines in the Raman spectra of the proposed simplified structure of the charge- and orbital-ordered $La_{0.5}Ca_{0.5}MnO_3$ finely twinned single crystal Ref. 5. In fact, Table II can be used for determination of the symmetry of the Raman lines in any case of a finely twinned quasicubic single crystal consisting of orthorhombic domains having a structure with D_{2h} symmetry and if the x, y, and z orthorhombic axes are parallel to the [101], [010], and $[\overline{1}01]$ quasicubic directions, respectively.

[10] The intensity ratio of an A_g mode in the general case is $I_{xx}:I_{y'x'}:I_{x'x'}:I_{yx}=[(a+c)^2+2b^2]:\frac{1}{4}(a-2b+c)^2:[a^2+c^2+\frac{1}{4}(a+2b+c)^2]:\frac{1}{2}(a-c)^2$, where a, b, and c are the nonzero

components of the corresponding Raman tensor.

[11] There is an additional special case, where the A_g Raman tensor components are $a=-c$, $b=0$. Such an A_g mode will have the same intensity ratio as B_{1g} and B_{3g} modes and it will be indistinguishable from them. Based on the LDC's, however, none of the A_g modes can be connected to a line with such a type of Raman tensor.

[12] M.V. Abrashev, V.G. Ivanov, M.N. Iliev, R.A. Chakalov, R.I. Chakalova, and C. Thomsen, Phys. Status Solidi B **215**, 631 (1999).

[13] E. Liarokapis, Th. Leventouri, D. Lampakis, D. Palles, J.J. Neumeier, and D.H. Goodwin, Phys. Rev. B **60**, 12 758 (1999).

[14] E. Granado, J.A. Sanjurjo, C. Rettori, J.J. Neumeier, and S.B. Oseroff, Phys. Rev. B **62**, 11 304 (2000).

[15] E. Granado, N.O. Moreno, H. Martinho, A. Garcia, J.A. Sanjurjo, I. Torriani, C. Rettori, J.J. Neumeier, and S.B. Oseroff, Phys. Rev. Lett. **86**, 5385 (2001).

[16] R.W.G. Wickoff, in *Crystal Structures*, 2nd ed. (Interscience, New York, 1964), Vol. 2, p. 407.

[17] W.E. Pickett and D.J. Singh, Phys. Rev. B **53**, 1146 (1996).

[18] A.M. Glazer, Acta Crystallogr., Sect. B: Struct. Crystallogr. Cryst. Chem. **28**, 3384 (1972).

[19] For the $Imma$ structure it is true if $z_A = z_{O(1)}$.

[20] J. Rodriguez-Carvajal, M. Hennion, F. Moussa, A.H. Moudden, L. Pinsard, and A. Revcolevschi, Phys. Rev. B **57**, R3189 (1998).

[21] P.G. Radaelli, G. Iannone, M. Marezio, H.Y. Hwang, S.-W. Cheong, J.D. Jorgensen, and D.N. Argyriou, Phys. Rev. B **56**, 8265 (1997).

[22] S. Sasaki, C.T. Prewitt, and R.C. Liebermann, Am. Mineral. **68**, 1189 (1983).

[23] Ph. Daniel, M. Rousseau, A. Desert, A. Ratuszna, and F. Ganot, Phys. Rev. B **51**, 12 337 (1995).

[24] Such a case where an A_g mode in an orthorhombic structure has corresponding B_{1g} mode in simpler tetragonal structure is the "quasi-B_{1g} out-of-phase" oxygen mode in $\mathrm{YBa_2Cu_3O_7}$ (Ref. 25).

[25] R. Liu, C. Thomsen, W. Kress, M. Cardona, B. Gegenheimer, F.W. de Wette, J. Prade, A.D. Kulkarni, and U. Schröder, Phys. Rev. B **37**, 7971 (1988).

[26] H.C. Gupta and P. Ashdhir, J. Raman Spectrosc. **30**, 493 (1999).

[27] D.J. Durben, G.H. Wolf, and P.F. McMillan, Phys. Chem. Miner. **18**, 215 (1991).

[28] M.V. Abrashev, A.P. Litvinchuk, M.N. Iliev, R.L. Meng, V.N. Popov, V.G. Ivanov, R.A. Chakalov, and C. Thomsen, Phys. Rev. B **59**, 4146 (1999).